HHS Public Access

Author manuscript

Cell Rep. Author manuscript; available in PMC 2017 November 22.

Published in final edited form as:

Cell Rep. 2017 September 05; 20(10): 2341–2356. doi:10.1016/j.celrep.2017.08.034.

Autophagy-independent lysosomal targeting regulated by ULK1/2-FIP200 and ATG9

Jonathan M. Goodwin[1], **William E. Dowdle**[1,§], **Rowena DeJesus**[1], **Zuncai Wang**[1], **Philip Bergman**[1], **Marek Kobylarz**[1], **Alicia Lindeman**[1], **Ramnik Xavier**[3], **Gregory McAllister**[1], **Beat Nyfeler**[2,*], **Gregory Hoffman**[1,*], and **Leon O. Murphy**[1,*]

[1]Novartis Institutes for Biomedical Research, 181 Massachusetts Avenue, Cambridge, MA 02139, USA [2]Novartis Institutes for Biomedical Research, Novartis Campus, CH-4056 Basel, Switzerland [3]Massachusetts General Hospital, Harvard Medical School, 55 Fruit Street, Boston, MA 02114, USA

SUMMARY

Iron is vital for many homeostatic processes and its liberation from ferritin nanocages occurs in the lysosome. Studies indicate that ferritin and its binding partner nuclear receptor coactivator-4 (NCOA4) are targeted to lysosomes by a form of selective autophagy. By using genome-scale functional screening we identify an alternative lysosomal transport pathway for ferritin that requires FIP200, ATG9A, VPS34 and TAX1BP1 but lacks involvement of the ATG8 lipidation machinery that constitutes classical macroautophagy. TAX1BP1 binds directly to NCOA4 and is required for lysosomal trafficking of ferritin under basal and iron depleted conditions. Under basal conditions ULK1/2-FIP200 controls ferritin turnover but its deletion leads to TAX1BP1-dependent activation of TBK1 which regulates redistribution of ATG9A to the Golgi enabling continued trafficking of ferritin. Cells expressing an Amyotrophic Lateral Sclerosis (ALS)-associated TBK1 allele are incapable of degrading ferritin suggesting a novel molecular mechanism that explains the presence of iron deposits in patient brain biopsies.

Graphical Abstract

*Correspondence to: beat.nyfeler@novartis.com, greg.hoffman@novartis.com, leonogmurphy@gmail.com.
§Present address: Denali Therapeutics, 151 Oyster Point Blvd., Floor 2, South San Francisco, CA, 94080.
Lead Contact: Leon Murphy, leonogmurphy@gmail.com

AUTHOR CONTRIBUTIONS:

Conceptualization, J.M.G., W.E.D., G.H., B.N., and L.O.M., Methodology, J.M.G., W.E.D., R.D., G.H., B.N., and L.O.M., Investigation, J.M.G., W.E.D., R.D., Z.W., P.B., and M.K., Formal Analysis, J.M.G., W.E.D, A.L., G.M., G.H., B.N., and L.O.M., Writing – Original Draft, J.M.G., G.H., B.N., and L.O.M., Writing – Review & Editing, J.M.G., R.X., G.H., B.N., and L.O.M., Funding Acquisition, G.H., B.N., and L.O.M., Visualization, J.M.G, G.M., G.H., and B.N., Resources, R.D. and Z.W., Supervision, G.H., B.N., and L.O.M.

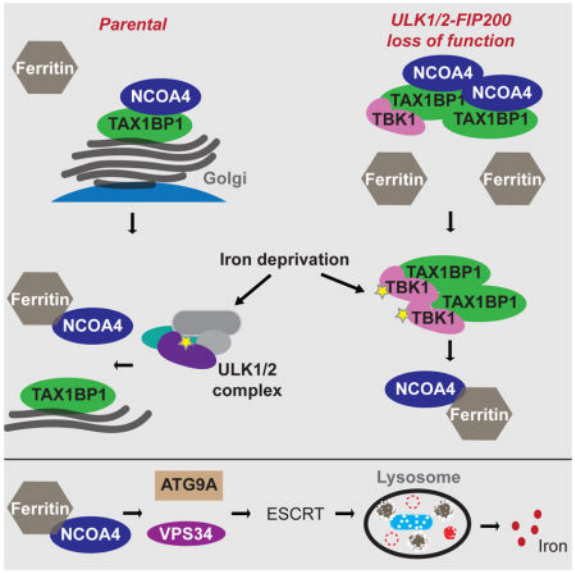

Keywords

NCOA4; ferritinophagy; autophagy; ULK1/2; TBK1; ALS; TAX1BP1; ATG9A; pooled CRISPR screen; trafficking

INTRODUCTION

Sufficient levels of intracellular iron govern essential biological processes such as DNA synthesis and adenosine triphosphate (ATP) production, and iron serves as a crucial cofactor in numerous biochemical reactions (Pantopoulos et al., 2012; Bogdan et al., 2016). Excess iron, however, is highly reactive and can promote cell death through generation of reactive oxygen species. Proteins that directly bind iron, such as ferritin, protect the cell from iron-induced stress and allow for rapid adaptation to changing intracellular concentrations and demand (Rouault, 2006). Ferritin is comprised of heavy and light chains which form a protective cage to hold free iron in a redox-inactive state (Theil, 2011). When iron is limiting, ferritin can be rapidly degraded in the lysosome which then releases free iron to restore homeostasis (Asano et al., 2011; De Domenico et al., 2009). Certain neuropathies and neurodegenerative disorders display evidence of ferritin accumulation and deregulation of cellular iron homeostasis (Goodall et al., 2008; Zheng et al., 2016; Ward et al., 2014) yet the precise molecular machinery that regulates ferritin degradation remain largely unknown.

Macroautophagy (herein referred to as autophagy) is a pathway through which organelles, ubiquitinated proteins, intracellular pathogens, and protein aggregates can be encapsulated within a double membrane vesicle and targeted to the lysosome for degradation (Mizushima et al., 2011). This conserved cellular recycling pathway is essential to maintain homeostasis upon diverse cellular stress conditions, such as nutrient starvation, mitochondrial damage, and pathogen infection (Kroemer et al., 2010). Recent work suggests that rather than proceeding as a bulk, non-selective process, specific targeting of cargo to the autophagosome is facilitated by a group of proteins known as autophagy cargo adaptors

(Deretic et al., 2013; Stolz et al., 2014). Cargo adaptors possess two defining features; the ability to bind ATG8 family members on the growing autophagosome through an LC3-interaction region (LIR) domain, and an ubiquitin interacting domain for cargo recruitment (Birgisdottir et al., 2013; Bjorkoy et al., 2005). Within this class of proteins, distinct cargo receptors mediate distinct types of selective autophagy. In addition, many receptors are also known to have core functions in immune signaling and metabolic homeostasis independent of cargo receptor function (Komatsu et al., 2010; Duran et al., 2011; Shembade et al., 2010). Intense efforts have focused on defining the specificity of cargo-cargo receptor interactions (Wild et al, 2011; Lazarou et al., 2015; Heo et al., 2015) and decoding the regulatory mechanisms that provide separation of distinct adaptor function within the cell.

Nuclear receptor co-activator 4 (NCOA4) was identified by our group and others as a ferritin binding partner required for its lysosomal turnover, suggesting NCOA4 functions as a cargo receptor for ferritin (Mancias et al., 2014; Dowdle et al, 2014). However, NCOA4 lacks both the defining LIR and ubiquitin binding domains, suggesting that it regulates ferritin degradation by a distinct mechanism. Here, we have employed pooled CRISPR screening approaches to identify core regulators of NCOA4 function. Interestingly, we have discovered that NCOA4 regulates ferritin degradation through a unique process dependent on core members of the autophagy initiation machinery, but independent of the ATG8 lipidation machinery that defines classical autophagy. We have identified TAX1BP1 as a direct interactor of NCOA4 required for lysosomal ferritin flux, independent from its role as an autophagy cargo receptor. Furthermore, we have identified a compensatory relationship between two kinases governing ferritin turnover, providing insight into observations of altered iron homeostasis in neurodegenerative disease states.

RESULTS

Pooled CRISPR screening reveals ferritin turnover is independent of macroautophagy

To define the mechanisms underlying NCOA4 regulation of ferritin turnover, we performed a pooled CRISPR (clustered regularly interspaced short palindromic repeats) screen to identify genes that modulate the abundance of GFP-NCOA4 in H4 neuroglioma cells (Figure 1A). H4 Cas9 GFP-NCOA4 cells stably express Cas9 and the GFP-NCOA4 fusion protein and treatment with the v-ATPase inhibitor Bafilomycin A1 (BafA1) confirmed the lysosomal trafficking of the reporter (Figure 1B). The CRISPR-based screening paradigm has been previously applied to GFP-p62 and comprehensively mapped the machinery of mammalian autophagy, thereby validating the approach (DeJesus et al., 2016). We identified numerous components of the HOPS, GARP and ESCRT complexes as specific regulators of NCOA4 (Figure 1D), revealing an unexpected role for vacuolar protein sorting (VPS) components in ferritin turnover. Select autophagy genes, such as *ATG9*, *RB1CC1* (FIP200), or *PIK3C3* (VPS34), robustly scored in the GFP-NCOA4 screen but surprisingly the enrichment for other autophagy components was less pronounced than for GFP-p62 (Figures 1C and 1D). To test the autophagy dependence of NCOA4 turnover, we created clonal CRISPR knockout H4 cell lines. Analysis of endogenous NCOA4 flux revealed that turnover was completely blocked uniquely upon *ATG9A* deletion (Figure 1E). Knock out of *RB1CC1* (FIP200) showed a partial block and distinct pattern with accumulated NCOA4 exhibiting a

slight mobility shift (Figure 1E). However, deletion of the autophagy genes *ATG16L1*, *ATG14*, *ATG7*, and *ATG3* did not robustly affect the basal levels of NCOA4, nor its accumulation upon treatment with BafA1 (Figure 1E). Importantly, lysosomal flux of p62 was fully blocked across our knockout panel, consistent with inhibition of autophagy (Figure 1E). We previously reported that NCOA4 protein levels were elevated in *ATG7*$^{-/-}$ DLD1 cells (Dowdle et al., 2014), however upon imaging, we failed to detect NCOA4 in p62-positive punctate structures that result from blocked autophagosome formation in both H4 and DLD1 cells (Figures S1C and S1A). Furthermore, NCOA4 can still undergo continued lysosomal degradation in the absence of ATG7 in DLD1 cells as evidenced by the accumulation upon BafA1 treatment (Figure S1B).

Treatment of cells with iron chelators depletes cellular iron and stimulates lysosomal ferritin degradation. Deletion of ATG9A was sufficient to completely block ferritin degradation and lysosomal localization, whereas deletion of FIP200 resulted in a partial block of ferritin turnover (Figure 1G). NCOA4 and ferritin colocalize in large puncta in ATG9A knockout cells, whereas a partial defect in ferritin traffic is observed in FIP200 knockout cells (Figure 1F). Importantly, deletion of ATG7 or ATG3 had no impact on ferritin turnover, confirming that ferritinophagy is independent from classical macroautophagy in H4 cells (Figure 1G and Figure S1F). To confirm that the partial effects of FIP200 knockout reflected its role as a component of the ULK complex, we assayed the function of ULK1 and ULK2 in ferritin turnover directly. ULK1 knockout or ULK2 knockdown H4 cells displayed a slight accumulation of ferritin under basal conditions, and this effect was enhanced by knock down of ULK2 in the ULK1 knockout background (Figure S1G). Accordingly, while depletion of ULK1 or ULK2 alone had mild effects on ferritin turnover, combined ULK1/ULK2 loss of function strongly blocked ferritin degradation upon iron depletion (Figure S1G). The ferritin response to iron depletion is mediated by the endolysosomal system in H4 cells, as treatment with BafA1 or the VPS34 inhibitor PIK-III was able to block turnover in both parental and FIP200 knockout cells (Figure S1D). Further studies in mouse embryonic fibroblasts (MEF) revealed ferritin degradation to be partially dependent on FIP200, but completely independent from ATG7-mediated autophagy, consistent with our findings in H4 cells (Figure S1E). Collectively, these observations highlight a divergence in the mechanisms governing turnover of p62 versus NCOA4/ferritin and suggest that ferritin turnover does not depend on the ATG8 lipidation machinery nor does it fit the current definition of selective autophagy.

Requirement of ESCRT proteins for lysosomal flux of NCOA4 and ferritin

As discussed above, the GFP-NCOA4 screen uniquely identified several genes that map to the endosomal sorting complex required for transport (ESCRT) pathway (Figure 2A). To specifically assay the ESCRT components, we made CRISPR knockout cell lines using the top gRNA sequence characterized in the GFP-NCOA4 screen and assayed effects on endogenous NCOA4 and ferritin. Deletion of these core ESCRT proteins, namely Hrs, PTPN23, and USP8 caused significant accumulation of both proteins compared to disruption of the autophagy pathway (Figure 2B), suggesting that the ESCRT pathway regulates ferritin lysosomal flux in H4 cells. In support of these findings, we found that deletion of Hrs (*HGS*) using two independent gRNA sequences resulted in a block in ferritin turnover upon iron

chelation (Figure 2C). Ferritin also displayed a punctate localization pattern in Hrs knockout cells, unlike the perinuclear distribution found in CTRL cells (Figure 2D).

USP8 enzyme function in the ESCRT pathway balances the degradation and recycling of ubiquitinated cargo, acting proximal to lysosomal commitment (Ali et al., 2013; Berlin et al., 2010). USP8 knockout H4 cell lines exhibited a robust accumulation of ferritin and NCOA4, as well as defective ferritin degradation (Figures 2E and S2C). Importantly, basal levels of p62 appear largely unaffected by USP8 deletion, providing an example of the distinct regulation of NCOA4 compared to a classical autophagy cargo receptor (Figure 2E). Examination of ferritin localization by immunofluorescence in USP8 knockout cells revealed a striking accumulation in LAMP2-positive structures, likely representative of a late endosomal or lysosomal compartment (Figure S2B). The requirement for USP8 in regulating ferritin turnover was further confirmed in U2OS cells using a siRNA approach (Figure 2F). Importantly, USP8 knock down did not impair LC3 conversion upon mTOR inhibition (Figure S2A), further indicating that our observed effects on NCOA4 and ferritin protein levels do not reflect a general block in autophagic capacity.

To further investigate USP8, we took a pharmacological validation approach using a previously published USP8 inhibitor (Colombo et al., 2010). Upon iron chelation with DFX treatment, the USP8 inhibitor was able to efficiently block lysosomal degradation of ferritin (Figure 2G), consistent with our observations in USP8 knockout cells. Taken together, our data suggest that ferritin targeting to and turnover in the lysosome occurs independently of autophagy, yet requires key components of the ESCRT pathway.

Identification of TAX1BP1 as a core interactor of NCOA4 required for ferritin turnover

We prioritized hits from the NCOA4 CRISPR screen using phenotypic correlations provided by gene essentiality (Wang et al, 2017) which has the potential to identify critical pathway regulators likely to be proximal to NCOA4. Analysis of a large scale proliferation-based pooled shRNA screen encompassing 390 cell lines from the Cancer Cell Line Encyclopedia (CCLE) (McDonald III et al, 2017)(Figure 3A) uncovered TAX1BP1 as the strongest correlation to NCOA4 downregulation (Figure 3B). TAX1BP1 is a bona-fide autophagy cargo receptor (Tumbarello et al., 2015; Lazarou et al., 2015) and identified as a unique hit in the GFP-NCOA4 CRISPR screen (Figure 1C). We found that pulldown of FLAG-NCOA4 efficiently recovered endogenous TAX1BP1 and FTH1 in 293T cells (Figure 3C). TAX1BP1 and NCOA4 colocalize at the Golgi in parental H4 cells (Figure S3A), while ferritin is largely in LAMP2-positive structures without robust NCOA4 colocalization (Figures 3D and S1C). Inhibition of VPS34 results in increased NCOA4 colocalization with ferritin at the Golgi (Figures 3D and 3E), suggesting that transport of NCOA4-ferritin complexes originates from the Golgi. We next generated clonal TAX1BP1 knockout H4 cells using CRISPR. TAX1BP1 deletion was sufficient to completely disrupt NCOA4 and ferritin traffic to the lysosome, without impacting the lysosomal flux of the autophagy cargo receptor p62 (Figures 3D, 3F and S3D). Interestingly, TAX1BP1 knock out resulted in endogenous NCOA4 and ferritin accumulation in peripheral puncta (Figures 3D and S3D). We hypothesize that these are insoluble aggregates of NCOA4 and ferritin, as TAX1BP1 knock

out in H4 cells shifts ferritin to the insoluble fraction with accumulated NCOA4 (Figure S3B).

We next examined the behavior of TAX1BP1 across the autophagy knockout cell line panel. Deletion of *RB1CC1*, *ATG16L1*, *ATG14*, *ATG7*, and *ATG3* resulted in an accumulation of TAX1BP1, however, protein levels were further increased upon lysosomal inhibition with Bafilomycin A1 (Figure 3G). In contrast, deletion of *ATG9A* was able to completely block all lysosomal flux of TAX1BP1 (Figure 3G), similar to what was observed for NCOA4 and consistent with the requirement of ATG9A for ferritin turnover. NCOA4 colocalized with TAX1BP1 in a punctate distribution upon FIP200 or ATG9A knockout, yet was noticeably absent from TAX1BP1 puncta observed in ATG7 knockout cells (Figure 3H). This suggests a unique involvement of FIP200 and ATG9A independent from their role in regulating autophagy initiation.

To examine ferritin turnover upon iron depletion, we treated parental and TAX1BP1 knockout cells with DFX and found that TAX1BP1, in addition to NCOA4, is essential for ferritin degradation in the lysosome (Figures 3I and 3J). NCOA4 associated with ferritin even in the absence of TAX1BP1, suggesting that the NCOA4-ferritin interaction is not sufficient for ferritin degradation (Figure S3C). The role of TAX1BP1 in ferritin degradation was specific as knock out of the closely related autophagy cargo receptor NDP52 did not alter sensitivity to DFX (Figure S3E). To confirm that the role of TAX1BP1 was independent from autophagy, we reconstituted TAX1BP1 knockout cells with wild-type or two different LC3-interacting region (LIR)-domain mutants of TAX1BP1 (Tumbarello et al., 2015) (Figure S3G). Expression of wild-type TAX1BP1 or either mutant restored ferritin lysosomal localization (Figure S3H), suggesting a novel role for TAX1BP1 outside of autophagy and its known cargo receptor function. These data further show that the process of ferritin turnover requires the NCOA4 binding partner TAX1BP1, VPS34, ATG9A, and partially the ULK1/2-FIP200 complex in a new lysosomal targeting pathway distinct from ATG8-mediated selective autophagy.

Minipool CRISPR screen for regulators of endogenous TAX1BP1 identifies TBK1

Given the requirement of TAX1BP1 in ferritin turnover, we employed a focused CRISPR screening approach to identify critical regulators of TAX1BP1 in both parental and FIP200 knockout cells (Figure 4A and Figure 4B). For this purpose a CRISPR library comprising the top scoring hits from the genome-wide GFP-p62 and GFP-NCOA4 screens was generated (Figure 4A). We hypothesized that mechanisms involved in TAX1BP1-dependent ferritinophagy would be particularly evident in FIP200 knockout cells where potential autophagy mediated regulation of TAX1BP1 would be blocked. Steady-state levels of p62 were uncoupled from the entire autophagy pathway in FIP200 knockout cells (Figure S4A), validating this screening concept. Interestingly, TBK1 scored as the top regulator of TAX1BP1 abundance specifically in the FIP200 knockout background in our mini-pool screening assay (Figure 4C). Knock out of TBK1 did not affect levels of endogenous p62 in either the parental or FIP200 knockout H4 cells (Figure 4C), suggesting a specific regulation of TAX1BP1 outside of autophagy.

TBK1 selectively regulates TAX1BP1 in FIP200 knockout cells and is required for ferritin turnover

Consistent with our screening result, genetic and pharmacological inhibition of TBK1 (Bamborough et al., 2006) had a strong effect on levels of TAX1BP1 and NCOA4 but only in the absence of FIP200 (Figure 5A and Figure 5B). NCOA4 and TAX1BP1 were partially colocalized but also present in distinct puncta in FIP200 knockout cells (Figure 5C). However, FIP200 and TBK1 double knockout cells were characterized by complete colocalization of TAX1BP1 and NCOA4. In stark contrast to NCOA4, ferritin localization became diffuse upon combined FIP200 knock out and TBK1 depletion/inhibition, a phenotype similar to NCOA4 knock out (Figure 5D). Accordingly, pharmacological inhibition of TBK1 had a minimal effect on ferritin turnover in parental H4 cells but completely suppressed it in FIP200 or ATG13 knockout cells (Figure 5E and Figure 5F). This synergy was independent from inhibition of autophagy, as ferritin levels in ATG7 knockout cells were insensitive to TBK1 inhibition (Figure 5G). Critically, genetic or pharmacological inhibition of TBK1 had no effect on p62 levels (Figure 5B and 5E). Together, these observations suggest the ULK1/2-FIP200 complex regulates basal ferritin lysosomal flux and that in the absence of this complex, TBK1 is central for continual regulation of ferritin turnover.

TBK1 is activated upon ULK1/2-FIP200 complex disruption and drives ferritin lysosomal flux

The specific involvement of TBK1 in the FIP200 knockout background and the shared regulation of ATG9A by ULK1/2 and TBK1 prompted us to ask whether ULK complex loss of function led to an upregulation of TBK1 activity. Knock out of core complex components FIP200 or ATG13 was sufficient to cause an upregulation of active P-TBK1 (Figure 6A). Knock out of ULK1 showed no effect on TBK1 phosphorylation presumably due to the redundant function of ULK2 (Figure S1G). FIP200 knockout cells displayed large P-TBK1 puncta peripheral to the Golgi apparatus (Figure 6B). TBK1 activation is dependent upon transphosphorylation of TBK1 homodimers induced by local concentration (Ma et al., 2012; Helgason et al., 2013). Numerous adaptor proteins relevant in innate immune signaling, as well as mitophagy and xenophagy, have been shown to bind directly to and mediate TBK1 recruitment (Helgason et al., 2013; Thurston et al., 2009; Heo et al., 2015). We tested whether TAX1BP1 could serve as a TBK1 adaptor and found that TAX1BP1 pulldown in 293T cells could efficiently recover endogenous TBK1 (Figure 6C). We propose that the role of TAX1BP1 as a TBK1 adaptor protein contributes to the increase in P-TBK1 seen upon FIP200 deletion. Indeed, active P-TBK1 was observed in puncta that were TAX1BP1 positive (Figure 6E) and siRNA mediated depletion of TAX1BP1 was able to resolve the increase in P-TBK1 observed in FIP200 knockout cells, despite the persistence of large p62-positive aggregates (Figure 6D and Figure 6E).

To confirm the requirement of TBK1 kinase activity to drive ferritin turnover in the absence of FIP200, we rescued FIP200 and TBK1 double knockout cells with either WT or K38A (kinase-dead) TBK1 alleles (Figure 6F). Consistent with our previous results, modulation of TBK1 activity had little effect on ferritin turnover in parental cells; however FIP200 and TBK1 double knockout cells were fully defective in ferritin turnover. This effect could be

rescued by the addition of WT, but not K38A TBK1 (Figure 6F). Importantly, TBK1 activation was consistently observed upon iron depletion (Figure 6F). We further confirmed that TBK1 activity is upregulated in response to FIP200 knock out and can be stimulated by iron depletion in HEK293T cells, suggesting this was not specific to H4 cells (Figure 6H).

TBK1 directs ATG9A localization in the absence of FIP200

The complete block of ferritin turnover observed with FIP200 knock out and TBK1 inhibition was similar to that observed upon knock out of ATG9A. The ULK1 complex is known to regulate ATG9A trafficking as an essential initiation event in autophagy (Suzuki et al., 2015; Feng et al., 2016). We asked whether TBK1 could regulate ATG9A trafficking in FIP200 knockout cells. Under normal growth conditions, ATG9A is primarily localized to the Golgi compartment and is sensitive to the VPS34 inhibitor PIK-III (Figure S6A). Golgi localization is retained in FIP200 knockout cells, however combined FIP200 and TBK1 knock out resulted in sequestration of ATG9A away from the Golgi into punctate structures, an effect phenocopied by treatment with the TBK1 inhibitor (Figure 6G). To confirm the requirement of TBK1 kinase activity directly, we also examined ATG9A localization in FIP200-TBK1 double knockout cells reconstituted with either WT or KD-TBK1. Reconstitution of TBK1 rescued ATG9A localization dependent on kinase activity (Figure 6G). These data suggest that Golgi localization of ATG9A is important for ferritin turnover and can be driven by either the ULK1 complex or TBK1.

ALS mutant of TBK1 is defective in ferritin turnover

To our knowledge, this is the first description of TBK1 kinase activity being responsive to changes in cellular iron levels. Acute TBK1 activation occurred upon iron depletion and was dose-dependent (Figure 6I). TBK1 mutations were recently described in patients with amyotrophic lateral sclerosis (ALS) (Freischmidt et al., 2015; Oakes et al., 2017) and given that ferritin turnover in our FIP200 knockout system is driven entirely by TBK1, we chose to functionally characterize the ALS-associated E696K mutation in this pathway. While reconstitution of FIP200 and TBK1 double knockout cells with WT-TBK1 could rescue ferritin lysosomal localization, cells expressing the E696K-TBK1 allele exhibited a unique punctate ferritin distribution (Figure 6J). We further interrogated chelator-induced ferritin turnover and found that cells expressing E696K-TBK1 resulted in a pronounced accumulation NCOA4 and ferritin, despite retention of kinase activity (Figure 6K). In summary, we have discovered that TBK1 is responsive to cellular iron levels and disease-relevant mutations in TBK1 abrogate its ability to drive ferritin turnover to maintain iron homeostasis.

DISCUSSION

This study describes a novel lysosomal targeting pathway for ferritin which requires the ULK1/2-FIP200 complex, ATG9A, VPS34 and TAX1BP1 (Figure 7). Originally identified through yeast two-hybrid screening for interactors of the human T-lymphotropic virus type I (HTLV-1) Tax-1 protein (Gachon et al., 1998), TAX1BP1 was further characterized as an essential binding partner of A20 and potent negative regulator of both NF-kB and IRF3-mediated immune signaling (De Valck et al., 1999; Shembade et al, 2007). TAX1BP1 is

thought to function as an ubiquitin adaptor targeting A20 to specific immune signaling molecules for degradation (Shembade et al, 2008; Shembade et al., 2009). In addition to the ubiquitin adaptor properties, TAX1BP1 contains multiple LIR domains enabling its function as an autophagy cargo receptor in both mitophagy and xenophagy (Lazarou et al., 2015; Tumbarello et al. 2015). In the current study, we have identified a distinct function of TAX1BP1 in targeting ferritin to the lysosomes and find this process neither requires the ATG8 lipidation machinery nor the LIR domains of TAX1BP1 (Figure S1F; Figure 3D; Figure S3H). We hypothesize that TAX1BP1 functions as a critical binding chaperone of NCOA4, independent of its role as a selective autophagy receptor. NCOA4 is known to be highly insoluble *in vitro* with a high propensity for self-oligomerization (Monaco et al., 2001). Indeed, removal of TAX1BP1 results in the formation of insoluble puncta of NCOA4 and ferritin that are uncoupled from lysosomal trafficking, suggesting NCOA4-ferritin binding is not sufficient for turnover (Figures S3B–D). Furthermore, we found that while FIP200 and TBK1 double knockout resulted in diffuse ferritin localization, the colocalization between NCOA4 and TAX1BP1 was enhanced (Figures 5C and 5D). It will be interesting to test in future studies if the NCOA4-TAX1BP1 interaction can be genetically or pharmacologically regulated. Interestingly, immune stimulation by viral RNA was recently shown to induce degradation of TAX1BP1 (Choi et al., 2016) and future studies will determine whether this acute degradation of TAX1BP1 during an immune response also coordinates iron homeostasis. Separation of the numerous functions of TAX1BP1 should provide valuable insights into the interplay between intracellular iron trafficking and innate immunity.

Several previous reports suggest that ferritin degradation occurs via autophagy (Asano et al., 2011; Mancias et al., 2014; Dowdle et al., 2014). The use of unbiased CRISPR screening now reveals a lysosomal trafficking pathway that depends on the ULK1/2-FIP200 complex, ATG9A, VPS34, but none of the other classical autophagy genes. Knock out of ATG7 completely blocked lysosomal turnover of p62 but did not robustly affect lysosomal flux of ferritin in H4 or mouse embryonic fibroblasts (Figures S1E and S1F). Interestingly, the recently described LC3-associated phagocytosis pathway depends on ATG7, ATG3, ATG5, ATG12 and ATG16L1 but not the ULK1/2-FIP200 complex (Martinez et al., 2011; Martinez et al., 2015). Examples of variation within the autophagy signaling cascade as well as distinct functions of autophagy proteins outside of classical autophagy are increasingly being reported (Kimmey et al., 2015; Nishida et al., 2009), exemplified further by the perinatal lethality associated with $Atg5^{-/-}$ or $Atg7^{-/-}$ mice (Kuma et al., 2004) versus the early embryonic lethality in $FIP200^{-/-}$ embryos (Gan et al., 2006). Additionally, it was recently suggested that previously defined autophagic cargo such as damaged mitochondria can traffic to the lysosome completely independent of autophagy, utilizing the ubiquitin-binding, vesicle-targeting properties of the ESCRT-0 proteins (Hammerling et al, 2017). These findings highlight the complexity and overlap between lysosomal trafficking pathways and warrant further investigation into their specific regulation and potential therapeutic modulation.

By running a sensitized CRISPR screen in FIP200 knockout cells, this study uncovered a compensatory relationship between the ULK1/2 complex and TBK1 activation that is sufficient to retain ferritin lysosomal flux, but not p62-dependent selective autophagy. TBK1

mutations were recently discovered to be associated with ALS and fronto-temporal dementia (FTD) (Freischmidt et al., 2015). Interestingly, patients with ALS exhibit elevated levels of serum ferritin, potentially reflective of elevated stored iron (Goodall et al., 2008; Zheng et al., 2016). Our findings that the ALS-associated E696K allele of TBK1 results in substantial cellular ferritin accumulation and impaired lysosomal turnover suggest that TBK1 regulation of iron homeostasis could be particularly relevant in this setting. Recent studies describe a relationship between *C9orf72*, a gene frequently mutated in familial cases of ALS/FTD, and loss of ULK1 complex function (Webster et al., 2016). While we have observed a compensatory upregulation of TBK1 to retain lysosomal ferritin flux, the basal accumulation of ferritin upon FIP200 knock out suggests this process is less efficient. We hypothesize that even subtle efficiency changes due to ULK1/2-FIP200 complex loss of function could contribute to a significant accumulation of cellular ferritin over time and manifest as a disease phenotype. Further studies will aim to characterize ferritin trafficking in ALS-disease models and determine if therapeutic modulation of this pathway could help preserve neuronal function.

EXPERIMENTAL PROCEDURES

Antibodies and Chemicals

Antibodies used in this study: NCOA4, immunoblot (1:1000, sc-373739), and NCOA4, immunofluorescence (1:200, sc-28749) were from Santa Cruz Biotechnology. NCOA4, immunoprecipitation (1:250, A302-272A) was from Bethyl Laboratories. TAX1BP1 (1:1000 IB, 1:200 IF, #5105), FTH1 (1:1000 IB, #4393), NDP52 (1:1000 IB, #9036), TBK1 (1:1000 IB, #3504), P-TBK1 S172 (1:1000 IB, 1:200 IF, #5483), beta-Actin (1:10,000 IB, #3700), ULK1 (1:1000 IB, #8054), ATG13 (1:1000 IB, #13468), FIP200 (1:1000 IB, #12436), ATG9A (1:1000 IB, #13509), ATG7 (1:1000 IB, #8558), ATG5 (1:1000 IB, #12994), ATG3 (1:1000 IB, #3415), Hrs (1:1000 IB, #15087), USP8 (1:1000 IB, #11832), vinculin (1:10,000 IB, #13901), p62/SQSTM1 (1:200 IF, #7695), and anti-DYKDDDDK tag (1:10,000 IB, #14793) were from Cell Signaling Technology. Mouse monoclonal anti-TAX1BP1 (clone 2C3, 1:150 IF) was from Sigma-Aldrich. Rabbit anti-ferritin (Rockland, 200-401-090-0100) was used for immunofluorescence and for FACS analysis (1:200). Rabbit anti-ATG9A (EPR2450(2)) was from Abcam and used for immunofluorescence (1:200). Rabbit anti-PTPN23 (1:1000 IB, 10472-1-AP) was from ProteinTech Group. Mouse anti-p62 (1:2500 IB, 1:500 IF, #610833) was from BD Biosciences. Mouse anti-LC3 was from MBL (1:200 IF, #M115-3).

The following chemicals were used: Deferasirox (DFX, 30 uM) and PIK-III (5 uM) were from Novartis Pharmaceuticals. Bafilomycin A1 (50 nM) was from Sigma Aldrich. AZD8055 (0.5 uM) was purchased from Selleckchem. TBK1 inh was synthesized in-house and has been previously published (Bamborough et al., 2006). The USP8 inhibitor was “compound 5a” from Colombo et al., 2010. All treatments were performed for 18 hr unless otherwise noted.

Mammalian cell culture

Cell lines used in this study were U2OS, H4, HEK293T, and DLD1 were obtained from the Novartis Cell Databank. Cell lines were confirmed by SNP analysis and verified to be mycoplasma-free by routine testing. All cells were cultured in a humidified incubator at 37°C and 5% CO_2. DLD1 wild-type and *ATG7*$^{-/-}$ were previously described (Dowdle et al., 2014). Cell culture reagents were obtained from Invitrogen unless otherwise specified. Cells were grown in Dulbecco's Modified Eagle's Medium (DMEM) supplemented with 10% fetal bovine serum and 1% penicillin/streptomycin. Mouse embryonic fibroblasts (MEF) were engineered to express Cas9 through lentiviral transduction of pNGx-LV-004 described below.

Generation of cDNA overexpression cell lines

To generate stable cDNA overexpression lines, cDNAs bearing the indicated mutations and the wild-type counterparts were synthesized by Genewiz except where noted. For TBK1 (NCBI), all constructs included an N-terminal FLAG epitope tag and contained wobble mutations to render the cDNA insensitive to the TBK1-g1 sgRNA. For TAX1BP1 (NCBI), all constructs included an N-terminal MYC epitope and the cDNA sequence was codon optimized. Constructs were then subcloned into the pXP1510 lentiviral vector, allowing for cDNA expression driven by the EF1-alpha promoter. To generate stable cell lines, 8×10^5 293T cells were plated in 6-well plates. The next day, cells were transfected with lentiviral packaging mix (1 ug ΔVPR (Δ8.9) and 0.25 ug VSV-G) along with 1 ug of the pXP1510 vector using FuGene 6 (Promega). Supernatant was removed from 293T cells after 48 hr, centrifuged at 2000 rpm for 5 min and then syringe filtered using a 0.45 um filter (Millipore). Polybrene was then added to a final concentration of 8 ug/ml and target cells were infected overnight. Cells were then allowed to recover for 24 hr in DMEM/10% FBS before being selected with 1 mg/ml neomycin (G418:Geneticin, Life Technologies) for 72 hr.

Generation of cell lines for pooled CRISPR screens

H4 GFP-SQSTM1 cells were generated by retroviral delivery of EGFP-SQSTM1 into human neuroglioma H4 cells as previously described (DeJesus and Moretti et al., 2016).

To generate GFP-NCOA4 reporter lines for FACS-based CRISPR screening, H4 parental cells were first infected with pRetro-X Tet-off Advanced (Clontech) followed by selection with G418 to generate H4.Tet-off cells. H4.Tet-off.GFP-NCOA4 (Clone B7) was selected for optimal expression. To generate reporter cell lines for GFP-based CRISPR screens, stable Cas9 expression was established via lentiviral delivery of the pNGx-LV-c004 Cas9 construct followed by blasticidin selection. For screening, blasticidin-resistant GFP-NCOA4 clones were picked, analyzed for Cas9 & GFP expression by western blot and immunofluorescence.

For the endogenous minipool screens characterizing p62 and TAX1BP1, parental H4.Cas9 or two *RB1CC1* (FIP200) knockout clones were used. Knockout clones were generated by transient transfection (Lipofectamine 2000, Life Technologies) of pNGx-LV-g006 plasmid containing sgRNA sequence against of the gene of interest and FLAG-Cas9. Populations

were then selected for 48 hr with puromycin. Cells were then expanded in the absence of selection, single-cell FACS sorted into 96-well plates, and clones expanded. Individual clones were then tested for knock out by western blot and puromycin sensitivity confirmed.

RNA interference

For siRNA mediated knock down, ON-TARGET pooled siRNA reagents were obtained from Dharmacon GE Life Sciences (TAX1BP1, L-016892-00-0005, ULK2, L-005396-00-0005, and nontargeting control, D-001810-10-05). Cells were transfected using Lipofectamine RNAiMAX (Life Technologies) using a reverse transfection protocol. siRNA knockdown was done for 72 hr to achieve sufficient suppression of protein expression.

Cell lysis, western blotting, and immunoprecipitation

For western blotting, cells were lysed in RIPA buffer (#9806, Cell Signaling Technology) supplemented with sodium dodecyl sulfate (SDS, Boston BioProducts) to 1% final concentration, and protease inhibitor tablets (Complete EDTA-free, Roche). Lysates were homogenized by sequential passaging through Qiashredder columns (Qiagen), and protein levels were quantified by Lowry DC protein assay (Bio-Rad). Proteins were denatured in 6X Laemmli SDS loading buffer (Boston BioProducts) at 100°C for 5 min and equivalent amounts separated on Tris-Glycine TGx SDS-PAGE gels (Bio-Rad). Proteins were transferred to nitrocellulose using standard methods and membranes were blocked in 5% non-fat dry milk (Bio-Rad) in TBS with 0.2% Tween-20 (Boston BioProducts). Primary antibodies were diluted in 5% bovine serum albumin (BSA, Cell Signaling Technology) in TBS with 0.2% Tween-20 and were incubated with membranes at 4°C overnight. HRP-conjugated secondary antibodies were diluted in blocking solution (1:10,000) and incubated with membranes at room temperature for 1 h. Western blots were developed using Pico or West Femto Super Signal ECL reagents (Pierce) and film (GEHealthcare).

For soluble and insoluble fractionation, cells were first lysed in Cell Lysis Buffer (#9803, Cell Signaling Technology) supplemented with protease inhibitor tablets (Roche) and Calyculin A (Cell Signaling Technology). After centrifugation, the supernatant was removed as the triton-X soluble fraction. The pellet was then resuspended in RIPA buffer (#9806, Cell Signaling Technology) supplemented with sodium dodecyl sulfate (SDS, Boston BioProducts) to 1% final concentration, and protease inhibitor tablets (Roche) as described above. The resulting lysate represented the triton-X insoluble fraction. As a reference total lysate, duplicate plates were lysed directly by RIPA lysis as described. Protein levels were quantified by Lowry DC protein assay (Bio-Rad).

For immunoprecipitations, cells were lysed in Cell Lysis Buffer (#9803, Cell Signaling Technology) supplemented with protease inhibitor tablets (Roche) and Calyculin A (Cell Signaling Technology). Lysates were clarified by centrifugation and equilibrated as described above. For FLAG IP, lysates were incubated with anti-M2 FLAG-conjugated agarose beads (Sigma-Aldrich) at 10 ul bed volume per 1 mg of protein and incubated for 1 hour at 4°C with gentle rocking. Immunoprecipitate was eluted by addition of 6X Laemmli SDS loading buffer at 100°C for 5 min.

Immunofluorescence

Cells were plated in 96-well glass bottom, black wall plates (GreinerOne, #655892) and grown overnight to 70% confluency. Treatments were performed as indicated. Cells were fixed for 10 min in either −20°C methanol or 4% paraformaldehyde (Electron Microscopy Sciences). Cells were blocked and permeabilized in a solution containing 1:1 Odyssey blocking buffer (LiCor)/PBS (Invitrogen) with 0.1% Triton X-100 (Sigma) and 1% normal goat serum (Invitrogen) for 1 h at room temperature. Primary antibodies were added overnight at 4°C in blocking buffer described above. After washing plates with PBS using an EL-406 plate washer (BioTek), secondary Alexa-conjugated antibodies (Life Technologies) were diluted 1:1,000 in blocking solution and applied for 1 h at room temperature. Cells were then washed again in PBS as described and imaged using an INCELL 6000 high-content imager. Images were then analyzed using HCS Explorer imaging software. Immunofluorescence quantitation was performed manually or through use of the Cell Profiler suite software (Carpenter at al., 2006).

Lentiviral CRISPR knockout generation

For validation experiments, individual sgRNAs were selected according to the screening results and cloned into the BbsI restriction site of either the pNGx-LV-g006 or pNGx-LV-g003 lentiviral backbone. gRNA sequences are listed in Supplementary Table 1. The g006 vector expresses the sgRNA of interest along with a FLAG-spCas9 protein, whereas the g003 vector expresses the sgRNA of interest along with an RFP marker. Briefly, 8×10^5 293T cells were plated in 6-well plates. The next day, cells were transfected with lentiviral packaging mix (1 ug ΔVPR (Δ8.9) and 0.25 ug VSV-G) along with 1 ug of the lentiviral vector using FuGene 6 (Promega). Supernatant was removed from 293T cells after 48 hr, centrifuged at 2000 rpm for 5 min and then syringe filtered using a 0.45 um filter (Millipore). Polybrene was then added to a final concentration of 8 ug/ml and target cells were infected overnight. Cells were then allowed to recover for 24 hr in DMEM/10% FBS before being selected with 2 ug/ml puromycin for 72 hr. Clonal lines were generated by single-cell FACS sorting and expansion.

gRNA Library Design & Construction

A genome wide gRNA library targeting 18,360 genes covering most protein coding genes was constructed as previously described (DeJesus and Moretti et al., 2016). The gRNA design was based on published sequences (Wang et al., 2014), selecting the 5 gRNAs most proximal to the transcriptional start site. For genes lacking published gRNA sequence information, new sgRNAs were designed for these targets that contained an NGG PAM motif, filtering for GC content greater than 40% and less than 80%, eliminating homopolymer stretches greater than 4, and removing any guides with off-target locations having fewer than 4 mismatches across the genome.

For the mini-pool library (Figure 4), single sgRNAs were picked for the top-ranked 300 genes in either the GFP low or GFP high category from either the GFP-NCOA4 or GFP-p62 genome-wide screens (DeJesus and Moretti et al., 2016). The mini-pool library was constructed using chip-based oligonucleotide synthesis (Custom Array) to generate spacer-encoding fragments that were PCR-amplified and cloned as a pool into the BbsI site of

pNGx-LV-g003 lentiviral plasmid. Sequencing of the plasmid pool showed robust normalization with >90% clones present at a representation of +/− 5-fold from the median counts in the pool.

Viral Packaging

For large scale production of the lentiviral gRNA library, 210×10^6 HEK293T cells were plated in cell stack (Corning) 24hrs prior to transfection. Cells were transfected according to previously described methods (Hoffman et al., 2014). For each cell stack, cells were transfected using 510.3 μL of TransIT reagent diluted 18.4 mL of OPTI-MEM that was combined with 75.6 μg of the gRNA library and 94.5 μg of the Cellecta packaging mix (containing the psPAX2 and pMD2 plasmids that encode Gag/Pol and VSV-G respectively). Virus was harvested at 72 hr post transfection, aliquoted, and frozen at −80C for later use. Viral titer was measured using the LentiX qPCR kit and was typically in the range of 5×10^6 TU/mL using this procedure.

Pooled CRISPR Screening

The GFP-NCOA4 reporter genome-wide CRISPR screen was performed as previously described for GFP-p62 (DeJesus et al., 2016).

For endogenous minipool screens, cells were harvested seven days post viral transduction and fixed with 4% paraformaldehyde for 20 min. Antibody staining was carried out according to the above immunofluorescence protocol. Cells were resuspended at 30 million cells/ml and single cells were sorted on and 25% low GFP and 25% high FITC levels. Approximately 4 million cells were collected from the low and high FITC bins.

Illumina library construction and sequencing

Genomic DNA from live cells was isolated using the QIAamp DNA Blood Maxi kit (Qiagen). Sample preparation and sequencing was carried out as previously described (DeJesus et al., 2016). Briefly, Illumina sequencing libraries were generated using PCR amplification with primers specific to the genome integrated lentiviral vector backbone sequence. The resulting Illumina libraries were purified using 1.8x SPRI AMPure XL beads (Beckman Coulter) following the manufacturer's recommendations and qPCR quantified using primers specific to the Illumina sequences using standard methods. Illumina sequencing libraries were pooled and sequenced with a HiSeq 2500 instrument (Illumina). The number of reads was adjusted to cover each sgRNA with approximately 1000 reads.

Data Analysis

Raw sequencing reads were aligned to the appropriate library using Bowtie (Langmead et al., 2009) allowing for no mismatches and counts were generated. Differential fold change estimates were generated using DESeq2 (Love et al., 2017) to compare the representation in the "low" gate to the "high" gate in the FACS sort. For gene-based hit calling, Redundant siRNA Activity (RSA) (Konig et al., 2007) and average or maximal fold changes were calculated across all reagents for a given gene.

Statistical Analysis

Immunofluorescence quantification was statistically analyzed using a two-tailed paired t-test, *p<.01.

Supplementary Material

Refer to Web version on PubMed Central for supplementary material.

Acknowledgments

We thank Sue Menon, Aron Jaffe, John Tallarico, Craig Mickanin, and Jeffrey Porter for support and feedback on the manuscript. We also thank Carsten Russ and John Reece-Hoyes for technical support. J.M.G., W.E.D., R.D., Z.W., P.B., M.K., A.L., G.M., G.H., B.N., L.O.M. are all employees of Novartis Pharmaceuticals. R.X. receives funding from the NIH.

References

Ali N, Zhang L, Taylor S, Mironov A, Urbe S, Woodman P. Recruitment of UBPY and ESCRT exchange drive HD-PTP-dependent sorting of EGFR to the MVB. Curr Biol. 2013; 23:453–61. [PubMed: 23477725]

Asano T, Komatsu M, Yamaguchi-Iwai Y, Ishikawa F, Mizushima N, Iwai K. Distinct mechanisms of ferritin delivery to lysosomes in iron-depleted and iron-replete cells. Mol Cell Biol. 2011; 31:2040–52. [PubMed: 21444722]

Bamborough P, Christopher JA, Cutler GJ, Dickson MC, Mellor GW, Morey JV, Patel CB, Shewchuk LM. 5-(1H-Benzimidazol-1-yl)-3-alkoxy-2-thiophenecarbonitriles as potent, selective, inhibitors of IKK-epsilon kinase. Bioorg Med Chem Lett. 2006; 16:6236–40. [PubMed: 16997559]

Berlin I, Schwartz H, Nash PD. Regulation of epidermal growth factor receptor ubiquitination and trafficking by the USP8-STAM complex. J Biol Chem. 2010; 285:34909–21. [PubMed: 20736164]

Birgisdottir AB, Lamark T, Johansen T. The LIR motif – crucial for selective autophagy. J Cell Sci. 2013; 126:3237–47. [PubMed: 23908376]

Bjørkøy G, Lamark T, Brech A, Outzen M, Perander M, Overvatn A, Stenmark H, Johansen T. p62/SQSTM1 forms protein aggregates degraded by autophagy and has a protective effect on huntingtin-induced cell death. J Cell Biol. 2005; 171:603–14. [PubMed: 16286508]

Bogdan AR, Miyazawa M, Hashimoto K, Tsuji Y. Regulators of iron homeostasis: New players in metabolism, cell death, and disease. Trends Biochem Sci. 2016; 41:274–86. [PubMed: 26725301]

Carpenter AE, et al. CellProfiler: image analysis software for identifying and quantifying cell phenotypes. Genome Biology. 2006; 7:R100. [PubMed: 17076895]

Choi YB, Shembade N, Parvatiyar K, Balachandran S, Harhaj EW. TAX1BP1 restrains virus induced apoptosis by facilitating Itch-mediated degradation of the mitochondrial adaptor MAVS. Mol Cell Biol. 2016; 37:e00422–16. [PubMed: 27736772]

Colombo M, Vallese S, Peretto I, Jacq X, Rain JC, Colland F, Guedat P. Synthesis and biological evaluation of 9-oxo-9H-indeno[1,2-b]pyrazine-2,3-dicarbonitrile analogues as potential inhibitors of deubiquitinating enzymes. ChemMedChem. 2010; 5:552–8. [PubMed: 20186914]

De Domenico I, Ward DM, Kaplan J. Specific iron chelators determine the route of ferritin degradation. Blood. 2009; 114:4546–51. [PubMed: 19671920]

De Valck D, Jin DY, Heyninck K, Van de Craen M, Contreras R, Fiers W, Jeang KT, Beyaert R. The zinc finger protein A20 interacts with a novel anti-apoptotic protein which is cleaved by specific caspases. Oncogene. 1999; 18:4182–90. [PubMed: 10435631]

DeJesus R, et al. Functional CRISPR screening identifies the ufmylation pathway as a regulator of SQSTM1/p62. eLife. 2016; 5:e17290. [PubMed: 27351204]

Deretic V, Saitoh T, Akira S. Autophagy in infection, inflammation and immunity. Nat Rev Immunol. 2013; 13:722–37. [PubMed: 24064518]

Dowdle WE, et al. Selective VPS34 inhibitor blocks autophagy and uncovers a role for NCOA4 in ferritin degradation and iron homeostasis in vivo. Nat Cell Biol. 2014; 16:1069–79. [PubMed: 25327288]

Duran A, Amanchy R, Linares JF, Joshi J, Abu-Baker S, Porollo A, Hansen M, Moscat J, Diaz-Meco MT. p62 is a key regulator of nutrient sensing in the mTORC1 pathway. Mol Cell. 2011; 44:134–46. [PubMed: 21981924]

Feng Y, Backues SK, Baba M, Heo JM, Harper JW, Klionsky DJ. Phosphorylation of Atg9 regulates movement to the phagophore assembly site and the rate of autophagosome formation. Autophagy. 2016; 12:648–58. [PubMed: 27050455]

Freischmidt A, et al. Haploinsufficiency of TBK1 causes familial ALS and fronto-temporal dementia. Nat Neurosci. 2015; 18:631–6. [PubMed: 25803835]

Gachon F, Peleraux A, Thebault S, Dick J, Lemasson I, Devaux C, Mesnard JM. CREB-2, a cellular CRE-dependent transcription repressor, functions in association with Tax as an activator of the human T-cell leukemia virus type 1 promoter. J Virol. 1998; 72:8332–7. [PubMed: 9733879]

Gan B, Peng X, Nagy T, Alcaraz A, Gu H, Guan JL. Role of FIP200 in cardiac and liver development and its regulation of TNFalpha and TSC-mTOR signaling pathways. J Cell Biol. 2006; 175:121–33. [PubMed: 17015619]

Goodall EF, Haque MS, Morrison KE. Increased serum ferritin in amyotrophic lateral sclerosis (ALS) patients. J Neurol. 2008; 255:1652–6. [PubMed: 18677636]

Hammerling BC, et al. A Rab5 endosomal pathway mediates Parkin-dependent mitochondrial clearance. Nat Commun. 2017; :8.doi: 10.1038/ncomms14050 [PubMed: 28364116]

Heo JM, Ordureau A, Paulo JA, Rinehart J, Harper JW. The PINK1-PARKIN Mitochondrial Ubiquitylation Pathway Drives a Program of OPTN/NDP52 Recruitment and TBK1 Activation to Promote Mitophagy. Mol Cell. 2015; 60:7–20. [PubMed: 26365381]

Helgason E, Phung QT, Dueber EC. Recent insights into the complexity of Tank-binding kinase 1 signaling networks: the emerging role of cellular localization in the activation and substrate specificity of TBK1. FEBS Lett. 2013; 587:1230–7. [PubMed: 23395801]

Hoffman GR, et al. Functional epigenetics approach identifies BRM/SMARCA2 as a critical synthetic lethal target in BRG1-deficient cancers. Proc Natl Acad Sci U S A. 2014; 111:3128–33. [PubMed: 24520176]

Kimmey JM, Huynh JP, Weiss LA, Park S, Kambal A, Debnath J, Virgin HW, Stallings CL. Unique role for ATG5 in neutrophil-mediated immunopathology during M. tuberculosis infection. Nature. 2015; 528:565–9. [PubMed: 26649827]

Komatsu M, et al. The selective autophagy substrate p62 activates the stress responsive transcription factor Nrf2 through inactivation of Keap1. Nat Cell Biol. 2010; 12:213–23. [PubMed: 20173742]

König R, et al. A probability-based approach for the analysis of large-scale RNAi screens. Nat Methods. 2007; 4:847–9. [PubMed: 17828270]

Kroemer G, Mariño G, Levine B. Autophagy and the integrated stress response. Mol Cell. 2010; 40:280–93. [PubMed: 20965422]

Kuma A, Hatano M, Matsui M, Yamamoto A, Nakaya H, Yoshimori T, Ohsumi Y, Tokuhisa T, Mizushima N. The role of autophagy during the early neonatal starvation period. Nature. 2004; 432:1032–6. [PubMed: 15525940]

Langmead B, Trapnell C, Pop M, Salzberg SL. Ultrafast and memory-efficient alignment of short DNA sequences to the human genome. Genome Biol. 2009; :10.doi: 10.1186/gb-2009-10-3-r25

Lazarou M, Sliter DA, Kane LA, Sarraf SA, Wang C, Burman JL, Sideris DP, Fogel AI, Youle RJ. The ubiquitin kinase PINK1 recruits autophagy receptors to induce mitophagy. Nature. 2015; 524:309–14. [PubMed: 26266977]

Love MI, Huber W, Anders S. Moderated estimation of fold change and dispersion for RNA-seq data with DESeq2. Genome Biol. 2014; :15.doi: 10.1186/s13059-014-0550-8

Ma X, et al. Molecular basis of Tank-binding kinase 1 activation by transautophosphorylation. Proc Natl Acad Sci. 2012; 109:9378–9383. [PubMed: 22619329]

Mancias JD, Wang X, Gygi SP, Harper JW, Kimmelman AC. Quantitative proteomics identifies NCOA4 as the cargo receptor mediating ferritinophagy. Nature. 2014; 509:105–09. [PubMed: 24695223]

Martinez J, Almendinger J, Oberst A, Ness R, Dillon CP, Fitzgerald P, Hengartner MO, Green DR. Microtubule-associated protein 1 light chain 3 alpha (LC3)-associated phagocytosis is required for the efficient clearance of dead cells. Proc Natl Acad Sci U S A. 2011; 108:17396–401. [PubMed: 21969579]

Martinez J, et al. Molecular characterization of LC3-associated phagocytosis reveals distinct roles for Rubicon, NOX2, and autophagy proteins. Nat Cell Biol. 2015; 17:893–90. [PubMed: 26098576]

McDonald ER III, et al. Project DRIVE: A Compendium of Cancer Dependencies and Synthetic Lethal Relationships Uncovered by Large-Scale, Deep RNAi Screening. Cell. 2017; 170:577–592. [PubMed: 28753431]

Mizushima N, Yoshimori T, Ohsumi Y. The role of Atg proteins in autophagosome formation. Annu Rev Cell Dev Biol. 2011; 27:107–32. [PubMed: 21801009]

Monaco C, et al. The RFG oligomerization domain mediates kinase activation and re-localization of the RET/PTC3 oncoprotein to the plasma membrane. Oncogene. 2001; 20:599–608. [PubMed: 11313992]

Nishida Y, et al. Discovery of Atg5/Atg7-independent alternative macroautophagy. Nature. 2009; 461:654–8. [PubMed: 19794493]

Pantopoulos K, Porwal SK, Tartakoff A, Devireddy L. Mechanisms of mammalian iron homeostasis. Biochemistry. 2012; 51:5705–24. [PubMed: 22703180]

Oakes JA, Davies MC, Collins MO. TBK1: a new player in ALS linking autophagy and neuroimflammation. Mol Brain. 2017; :10.doi: 10.1186/s13041-017-0287-x [PubMed: 28385162]

Rouault TA. The role of iron regulatory proteins in mammalian iron homeostasis and disease. Nat Chem Biol. 2006; 2:406–14. [PubMed: 16850017]

Shembade N, Harhaj NS, Liebl DJ, Harhaj EW. Essential role for TAX1BP1 in the termination of TNF-alpha-, IL-1- and LPS-mediated NF-kappaB and JNK signaling. EMBO J. 2007; 26:3910–22. [PubMed: 17703191]

Shembade N, Harhaj NS, Parvatiyar K, Copeland KG, Jenkins NA, Matesic LE, Harhaj EW. The E3 ligase Itch negatively regulates inflammatory signaling pathways by controlling the function of the ubiquitin-editing enzyme A20. Nat Immunol. 2008; 9:254–62. [PubMed: 18246070]

Shembade N, Parvatiyar K, Harhaj NS, Harhaj EW. The ubiquitin-editing enzyme A20 requires RNF11 to downregulate NF-kappaB signalling. EMBO J. 2009; 28:513–22. [PubMed: 19131965]

Shembade N, Ma A, Harhaj EW. Inhibition of NF-kappaB signaling by A20 through disruption of ubiquitin enzyme complexes. Science. 2010; 327:1135–9. [PubMed: 20185725]

Stolz A, Ernst A, Dikic I. Cargo recognition and trafficking in selective autophagy. Nat Cell Biol. 2014; 16:495–501. [PubMed: 24875736]

Suzuki SW, Yamamoto H, Oikawa Y, Kondo-Kakuta C, Kimura Y, Hirano H, Ohsumi Y. Atg13 HORMA domain recruits Atg9 vesicles during autophagosome formation. Proc Natl Acad Sci USA. 2015; 17:3350–5.

Theil EC. Ferritin protein nanocages use ion channels, catalytic sites, and nucleation channels to manage iron/oxygen chemistry. Curr Opin Chem Biol. 2011; 15:304–11. [PubMed: 21296609]

Thurston TL, Ryzhakov G, Bloor S, von Muhlinen N, Randow F. The TBK1 adaptor and autophagy receptor NDP52 restricts the proliferation of ubiquitin-coated bacteria. Nat Immunol. 2009; 10:1215–21. [PubMed: 19820708]

Tumbarello DA, Manna PT, Allen M, Bycroft M, Arden SD, Kendrick-Jones J, Buss F. The autophagy receptor TAX1BP1 and the molecular motor Myosin VI are required for clearance of Salmonella Typhimurium by autophagy. PLoS Pathog. 2015; 11:e1005174. [PubMed: 26451915]

Ward RJ, Zucca FA, Duyn JH, Crichton RR, Zecca L. The role of iron in brain ageing and neurodegenerative disorders. Lancet Neurol. 2014; 10:1045–60.

Wang T, Wei JJ, Sabatini DM, Lander ES. Genetic screens in human cells using the CRISPR-Cas9 system. Science. 2014; 343:80–4. [PubMed: 24336569]

Wang T, Yu H, Hughes NW, Liu B, Kendirli A, Klein K, Chen WW, Lander ES, Sabatini DM. Gene Essentiality Profiling Reveals Gene Networks and Synthetic Lethal Interactions with Oncogenic Ras. Cell. 2017; 168:890–903. [PubMed: 28162770]

Webster CP, et al. The C9orf72 protein interacts with Rab1a and the ULK complex to regulate initiation of autophagy. EMBO J. 2016; 35:1656–76. [PubMed: 27334615]

Wild P, et al. Phosphorylation of the autophagy receptor optineurin restricts Salmonella growth. Science. 2011; 333:228–33. [PubMed: 21617041]

Zheng Y, Gao L, Wang D, Zang D. Elevated levels of ferritin in the cerebrospinal fluid of amyotrophic lateral sclerosis patients. Acta Neurol Scand. 2016; doi: 10.1111/ane.12708

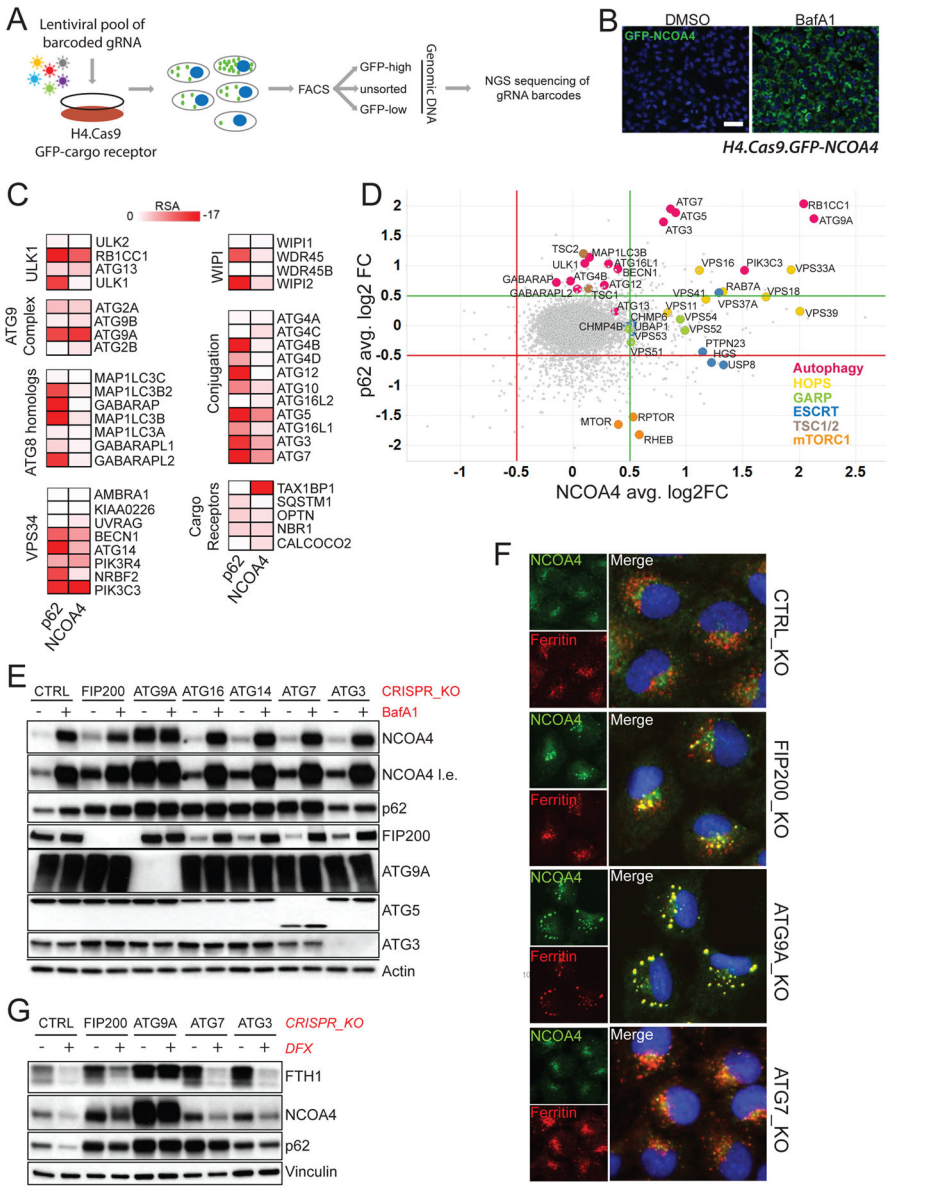

Figure 1. NCOA4 and ferritin lysosomal turnover is independent of classical macroautophagy

(**A**) Outline of FACS-based pooled CRISPR screening paradigm. GFP-reporter constructs undergo continued basal lysosomal flux, allowing the overall GFP abundance to serve as a readout for focused pathway regulators. (**B**) Response of the GFP-NCOA4 reporter construct in the H4.Cas9 screening line to Bafilomycin A treatment (25 nM) for 16 hr. Scale bar = 50 um. (**C**) Autophagy gene hit profile of GFP-NCOA4 and GFP-62 represented as a heatmap color-coded by RSA_up. (**D**) Overlap of GFP-NCOA4 and GFP-p62 screens. Compare plot of average log2 fold change of each screen with green and red lines representing significance cutoff for antagonism or agonism, respectively, of the GFP-reporter. Genes involved in lysosomal trafficking are highlighted. (**E**) Panel of clonal CRISPR knockout H4 cells encompassing the autophagy cascade treated with 25 nM Bafilomycin A1 (BafA1) for 18 hours. Lysates blotted with the indicated antibodies. (**F**) Immunofluorescence analysis of

NCOA4 and ferritin colocalization across a subset of autophagy CRISPR clonal knockout H4 cells. Representative images of 500 cells/genotype. (**G**) Treatment of H4 knockout panel with 30 uM deferasirox (DFX). Lysates blotted with the indicated antibodies.

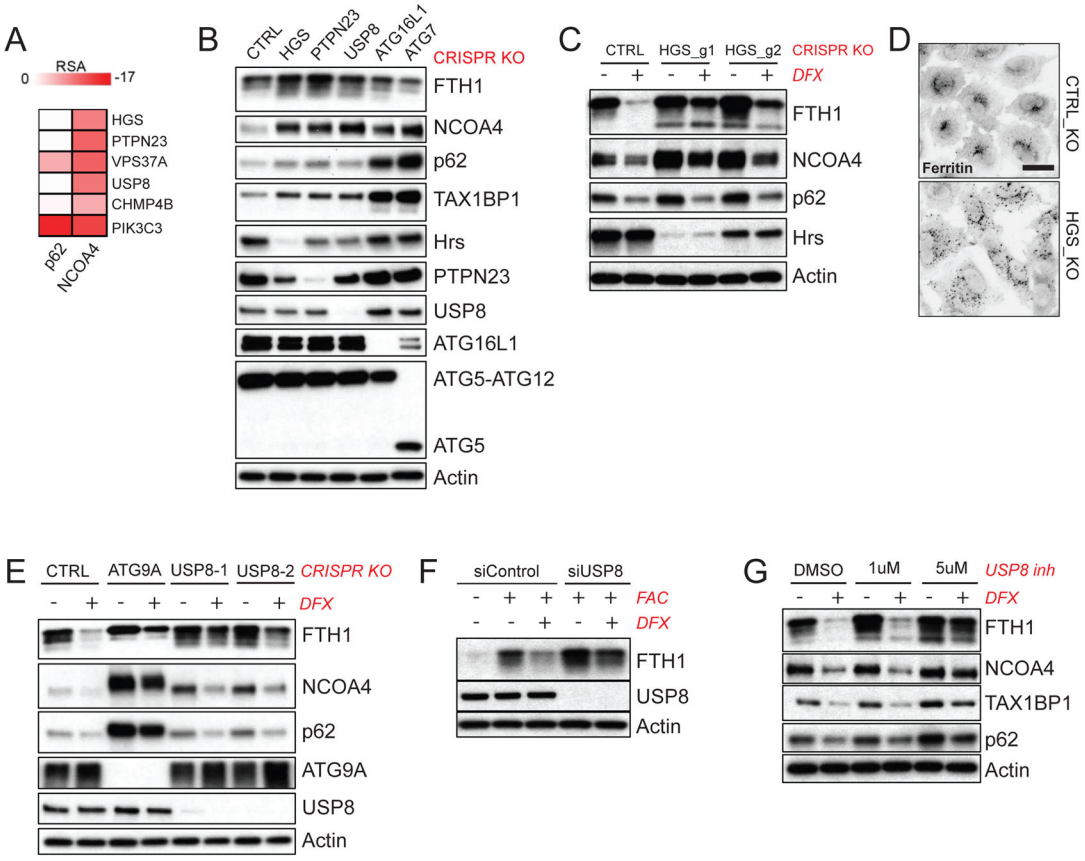

Figure 2. NCOA4 and ferritin lysosomal turnover requires components of the ESCRT pathway

(A) Heatmap representation of ESCRT hits in GFP-p62 vs GFP-NCOA4 screens. Heatmap color-coded by RSA_up. (**B**) CRISPR knockout panel comparing ESCRT hits with autophagy components. Lysates blotted with the indicated antibodies. (**C**) Depletion of Hrs (HGS) using two separate guides. Cells were edited for 7 days and treated for 18 hours with DFX (30 uM). Lysates blotted with the indicated antibodies. (**D**) Immunofluorescence analysis of ferritin localization in CTRL or HGS knockout H4 cells. Representative images of 500 cells/genotype. Scale bar = 30 uM. (**E**) Analysis of USP8 depletion effects on ferritin turnover. USP8 knockout cells were generated with two individual guides and treated with DFX (30 uM) for 18 hours. ATG9A knockout cells were included as a control. Lysates were blotted with the indicated antibodies. (**F**) U2OS cells were transfected with siRNA targeting *USP8*. 24 hr after transfection, cells were iron-loaded with 50 uM ferric ammonium citrate (FAC) for 18 hr. Cells were then washed twice and treated for 18 hr with 30 uM DFX. Lysates were immunoblotted with the indicated antibodies. (**G**) H4 cells were treated for 18 hr with a USP8 inhibitor (indicated dose) in combination with DFX (30 uM). Lysates were immunoblotted with the indicated antibodies.

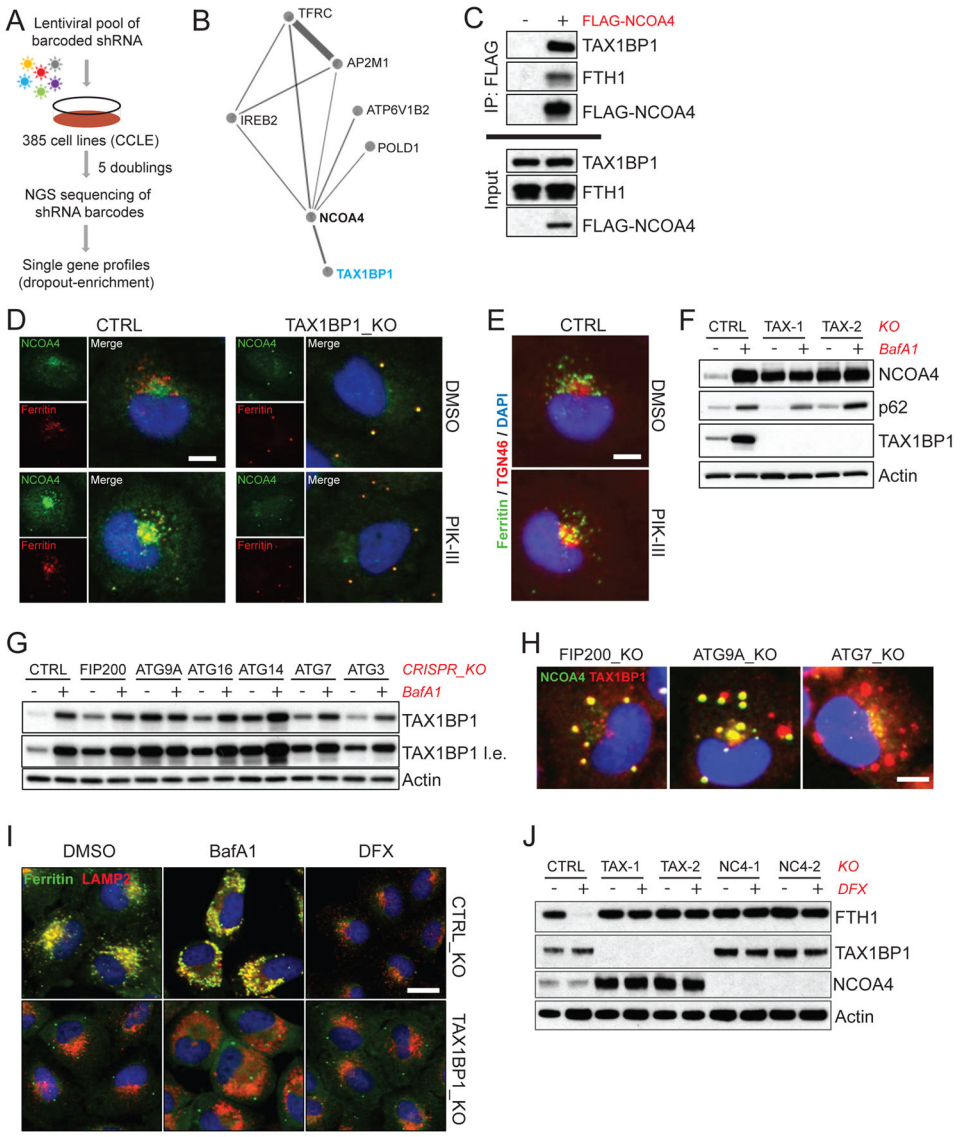

Figure 3. Identification of TAX1BP1 as an essential NCOA4-binding partner required for lysosomal ferritin turnover

(**A**) Schematic outline of cancer cell line encyclopedia (CCLE) shRNA sensitivity profiling effort. Library encoded shRNA against 7500 genes at a depth of 20 shRNA/gene. (**B**) Network map showing genetic correlation results for NCOA4. Line weight indicative of strength of correlation (Spearman's coefficient). TAX1BP1 represents most significantly correlated gene across library. (**C**) FLAG-NCOA4 pulldown in 293T blotted with the indicated antibodies for endogenous interactors. (**D**) Immunofluorescence analysis of NCOA4 and ferritin in H4 wild-type or clonal TAX1BP1 knockout cells. Cells were treated with 5 uM PIK-III for 18 hours. Representative images of 500 cells shown/condition. Scale bar = 10 um. (**E**) Immunolocalization of ferritin with the trans-golgi marker TGN46 in the presence or absence of 5 uM PIK-III. Representative images of 500 cells shown. Scale bar = 10 um. (**F**) Treatment of control or two individual clonal TAX1BP knockout H4 cell lines with BafA1 for 18 hours. Lysates blotted with the indicated antibodies. (**G**) Examination of

TAX1BP1 lysosomal flux across the H4 autophagy knockout panel treated with BafA1 for 18 hours. Lysates blotted with indicated antibodies. l.e.= long exposure. (**H**) NCOA4 and TAX1BP1 localization across indicated H4 knockout cells. Representative images of 500 cells shown. Scale bar = 10 um. (**I**) Immunofluorescence analysis of ferritin and LAMP2 to monitor lysosomal flux in wild-type or TAX1BP1 knockout cells. Representative images of 500 images shown. Scale bar = 50 um. (**J**) Immunoblot analysis of control or clonal NCOA4 or TAX1BP1 knockout H4 cell lines treated with 30 uM DFX for 18 hours. Lysates blotted with the indicated antibodies.

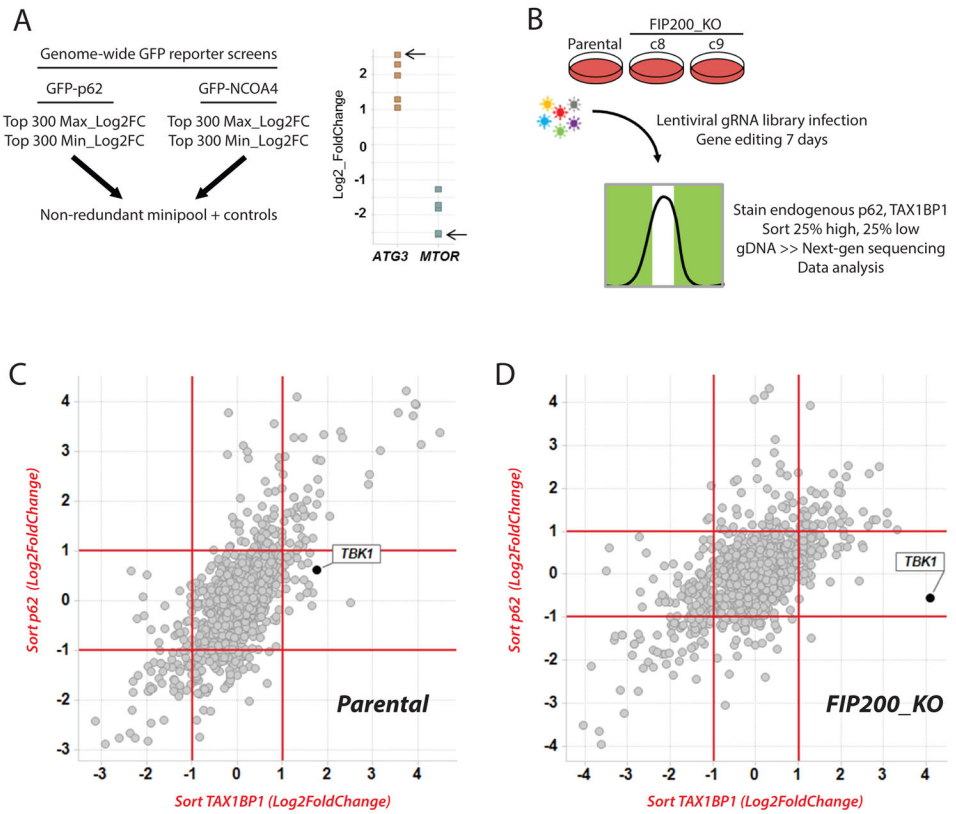

Figure 4. Focused CRISPR screening approach reveals TBK1 as a specific regulator of endogenous TAX1BP1 in FIP200 knockout cells

(**A**) Outline of minipool generation strategy. Top antagonists/agonists from GFP-p62 and GFP-NCOA4 genome-wide pooled CRISPR screens were identified. The gRNA sequence that produced the highest fold change in reporter abundance was chosen. Control sgRNA sequences targeting essential genes were included. (**B**) Outline of minipool screening strategy. Parental H4.Cas9 cells or two clonal FIP200 knockout derivatives were generated. Knockout cells were generated through transient transfection and clonal expansion to preserve puromycin resistance for screening libraries. Cells were harvested at seven days post-transduction, stained for endogenous p62 or TAX1BP1, and sorted on FITC abundance. (**C, D**) Compare plots of screening results in either parental (C) or FIP200 knockout (D) H4 cells. TBK1 was the top scoring guide in the regulation of TAX1BP1 in FIP200 knockout cells.

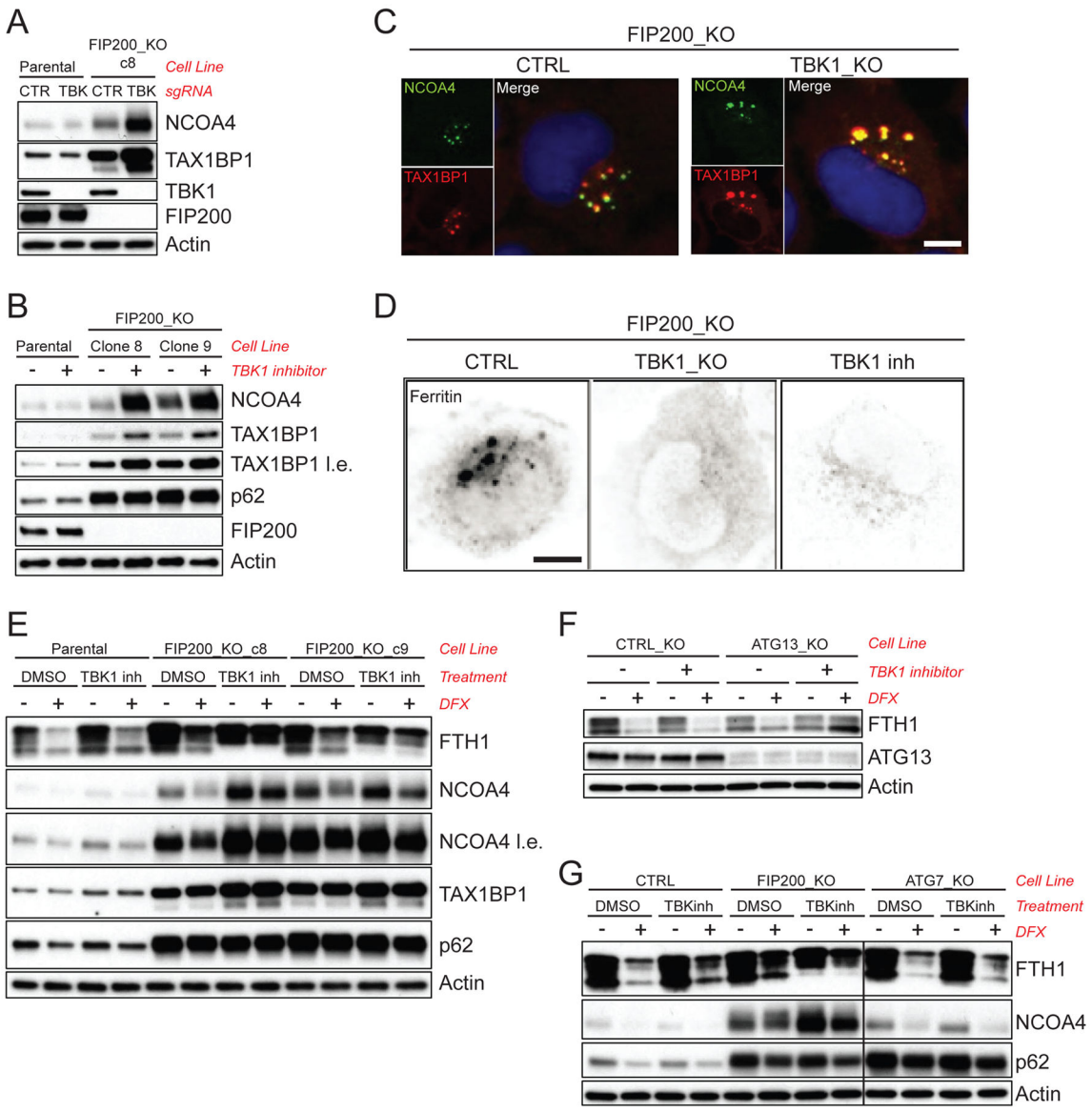

Figure 5. Genetic and pharmacological validation of TBK1 as a regulator of TAXBP1 with effects on ferritin turnover

(**A**) Generation of combined FIP200 and TBK1 double knockout cells to validate TBK1 screen result. Lysates were blotted with the indicated antibodies. (**B**) H4 control or two individual FIP200 clonal knockout cell lines were treated with a specific TBK1 inhibitor (TBK1 inh, 5 uM) for 18 hours. Lysates were blotted with the indicated antibodies. (**C**) Immunolocalization of TAX1BP1 and NCOA4 in response to either control or TBK1 knock out in FIP200-null background. Representative images of 500 cells shown. Scale bar = 10 um. (**D**) Immunofluorescence for ferritin in FIP200 knockout, FIP200/TBK1 double knockout, or FIP200 knockout + TBK1 inh treated (5 uM, 18 hr) H4 cells. Inverted contrast image shown representative of 500 cells/condition. Scale bar = 10 um. (**E**) Cotreatment of H4 control or individual H4 clonal FIP200 knockout cell lines with TBK1 inh (5 uM) and DFX (30 uM) for 18 hours. Lysates were blotted with the indicated antibodies. (**F**) Deletion

of an alternative core component of the ULK1 complex, ATG13, also results in TBK1 regulation of ferritin turnover. Cells of the indicated genotype were treated as in (d) and lysates blotted with the indicated antibodies. (**G**) TBK1 selectively regulates ferritin turnover in FIP200 knockout but not ATG7 knockout H4 cells. Cells were treated with 50 uM DFX and 5 uM TBK1 inh for 18 hr. Lysates were blotted with the indicated antibodies.

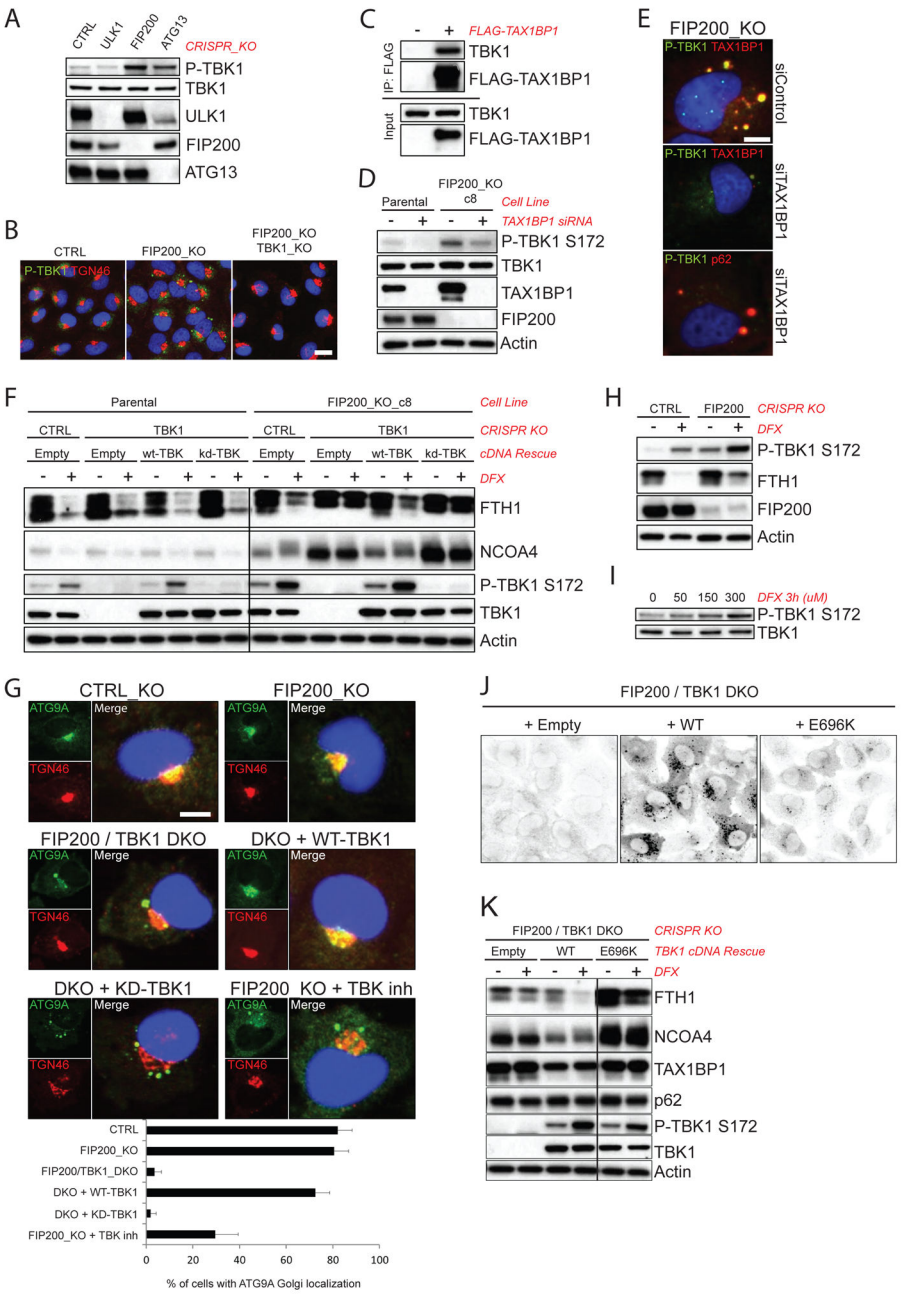

Figure 6. TBK1 is hyperactivated upon ULK complex loss-of-function and is sufficient to drive ferritin lysosomal degradation

(**A**) Pooled CRISPR knockout of the indicated genes harvested at 7 days post-transduction. Lysates were blotted with the indicated antibodies. (**B**) Immunofluorescence of endogenous P-TBK1 in either parental H4.Cas9 or clonal FIP200 knockout derivatives. FIP200/TBK1 double knockouts shown for antibody validation. Scale bar = 25 um. (**C**) Pulldown of epitope-tagged TAX1BP1 after transient transfection in HEK293T cells. Lysates blotted with the indicated antibodies. (**D**) siRNA knock down of TAX1BP1 for 72 hr using ONTarget pooled duplexes in either CTRL or FIP200 knockout H4 cells. Lysates blotted with the indicated antibodies. (**E**) Immunofluorescence for endogenous P-TBK1 in FIP200

knockout cells treated as in (d). TAX1BP1 counterstaining used to determine knockdown cells. Representative images of 500 cells shown. Scale bar = 10 um. (**F**) Examination of active TBK1 involvement in ferritin turnover. CTRL or FIP200 knockout H4 cells were transduced with lentivirus to express gRNA-resistant WT or K38A-TBK1. After selection, cells were then transduced with lentiviral gRNA vectors to deplete endogenous protein. Pooled knockout populations were selected for 7 days and then treated with 50 uM DFX for 20 hr. Lysates were blotted with the indicated antibodies. (**G**) Immunofluorescence for ATG9A and TGN46 localization in designated H4 cell lines. TBK1 inh treatment (5 uM) was for 18 hr. Representative images of 500 cells shown. Scale bar = 10 um. Quantification of ATG9A Golgi localization below. Cells were counted in 12 separate fields of view and data is expressed as the percent of cells/field with labeled phenotype. *p<.01 compared to FIP200_KO. Error bars represent S.D. (**H**) Confirmation of FIP200 knockout effect on active TBK1 in HEK293T cells. Pooled knockout lines were generated as in (a) and treated as in (d). Lysates blotted with the indicated antibodies. (**I**) Dose dependent activation of TBK1 in parental H4 cells treated with the indicated concentrations of DFX for 3 hr. Lysates blotted with indicated antibodies. (**J**) Immunofluorescence for endogenous ferritin in the indicated cell lines under basal conditions. Inverted contrast image shown representative of 500 cells/condition. Scale bar = 20 um. (**K**) Characterization of ferritin turnover in cells expressing the ALS mutant E696K-TBK1 construct in the FIP200 knockout background. cDNA expression and removal of endogenous protein performed as in (d). Lysates blotted with the indicated antibodies.

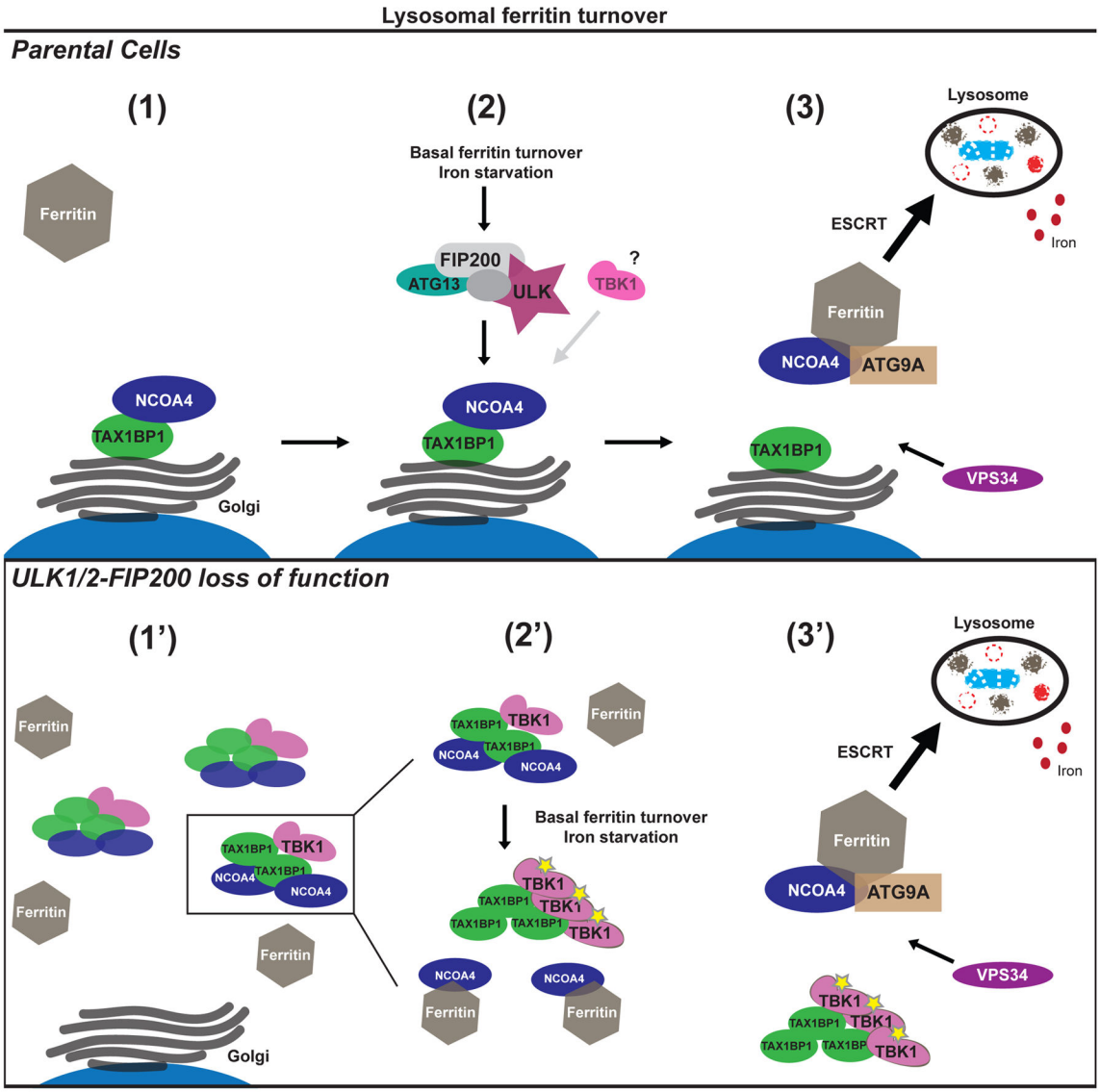

Figure 7. Model

Using a genome-wide CRISPR screening approach in parental H4 cells (**top**), TAX1BP1 was identified as a functional binding partner for NCOA4 and found to regulate ferritinophagy independently of its role as a selective autophagy cargo receptor (1). Under basal and iron-limited conditions (2) the ULK1/2-FIP200 complex regulates dissociation of NCOA4 from TAX1BP1 and allows it to bind ferritin. ATG9A (potentially the source of initial membrane to move NCOA4-ferritin complexes away from the Golgi), VPS34 (required for proper trafficking of ATG9A), and the ESCRT pathway are collectively required for trafficking of NCOA4 and ferritin to lysosomes ensuring the liberation of iron (3). Interestingly upon ULK1/2-FIP200 loss of function (**bottom**), the origin for the ferritin turnover pathway changes from the Golgi to cytosolic aggregates of TAX1BP1 (1′). These aggregates contain NCOA4 but are negative for ferritin. TAX1BP1 serves as an adaptor protein to mediate recruitment of TBK1 into the punctate structures, and TBK1 regulates basal ferritin flux as well as accelerated ferritin degradation upon iron depletion. We

hypothesize that TBK1 is able to regulate the TAX1BP1-NCOA4 interaction, allowing for regulated NCOA4-ferritin binding (2′). Furthermore, TBK1 plays an important role in regulating ATG9A trafficking to and from punctate TAX1BP1 structures which ultimately results in ferritin traffic to lysosomes through the downstream components required in parental H4 cells (3′).